FULL PAPER

Magnetic Resonance in Medicine 71:735–745 (2014)

High Speed 3D Overhauser-Enhanced MRI Using Combined b-SSFP and Compressed Sensing

Mathieu Sarracanie,[1,2] Brandon D. Armstrong,[1,2] Jason Stockmann,[1,2] and Matthew S. Rosen[1,2,3]*

Purpose: Overhauser-enhanced MRI is a promising technique for imaging the distribution and dynamics of free radicals. A key challenge for Overhauser-enhanced MRI is attaining high spatial and temporal resolution while simultaneously limiting resonator and sample heating due to the long, high power radio-frequency pulses needed to saturate the electron resonance.

Methods: The approach presented here embeds EPR pulses within a balanced steady state free precession sequence. Unlike other Overhauser-enhanced MRI methods, no separate Overhauser prepolarization step is required. This steady-state approach also eliminates the problem of time-varying Overhauser-enhanced signal and provides constant polarization in the sample during the acquisition. A further increase in temporal resolution was achieved by incorporating undersampled k-space strategies and compressed sensing reconstruction.

Results: We demonstrate $1 \times 2 \times 3.5$ mm^3 resolution at 6.5 mT across a $54 \times 54 \times 110$ mm^3 sample in 33 s while sampling 30% of k-space.

Conclusion: The work presented here overcomes the main limitations of Overhauser enhanced MRI as previously described in the literature, drastically improving speed and resolution, and enabling new opportunities for the measurement of free radicals in living organisms, and for the study of dynamic processes such as metabolism and flow. **Magn Reson Med 71:735–745, 2014. © 2013 Wiley Periodicals, Inc.**

Key words: 3D Overhauser MRI; free radicals; EPR; b-SSFP; compressed sensing

Imaging of free radicals has been used to investigate a number of important physiological processes such as the mapping of pO_2 (1–3), free radical distribution and metabolism (4–7), molecular imaging (8), and to monitor changes in local viscosity (9,10). Magnetic resonance imaging (MRI) is a powerful and noninvasive tool that provides excellent anatomical detail. However, MRI is sensitive to nuclear spins (typically ^{1}H of water) and cannot alone reveal spatial information about the distribution of free radical species. EPR imaging (11–17) reveals the spatial distribution of unpaired electron spins, but requires a separate reference MRI to determine where the free radicals are located within the sample. While EPR imaging is a sensitive technique, images have poor resolution due to broad EPR lines, and are usually time-inefficient due to the usual CW acquisition strategy. Overhauser-enhanced MRI (18–23; OMRI, also known as proton-electron double resonance imaging) exploits the dipolar coupling between the unpaired electron of the free radical and the ^{1}H nuclei of water to increase nuclear magnetization via dynamic nuclear polarization (DNP) and subsequently images the enhanced nuclear spin polarization with MRI. OMRI provides an excellent way to image free radical species as narrow NMR line widths enable imaging using reasonable-strength encoding gradients. OMRI also benefits from the ability to use traditional MRI sequences, though specialized hardware is needed to drive the electron spin resonance, and the sequences must be modified to allow for EPR saturation pulses.

A difficulty of OMRI is the need for high power radio-frequency (RF) to saturate the electron spins. Additionally, as EPR frequencies are two orders of magnitude higher than ^{1}H frequencies, a high frequency resonator is required, and this leads to high specific absorption rate (SAR) and limited penetration depth. For these reasons, OMRI is usually performed at a low- to intermediate magnetic field (5,22,24) or in a field-cycled setup (4,25). A typical field-cycled OMRI experiment begins at very low magnetic field ($\sim$5 mT) where EPR irradiation is applied for approximately the nuclear T_1 of the sample at the irradiation magnetic field. The magnetic field is then quickly ramped up to the imaging field and a line or plane of k-space data is acquired. The magnetic field is then ramped down for EPR irradiation and repolarization because the DNP signal decays with the ^{1}H nuclear T_1. Field-cycled OMRI helps to overcome both the hardware and penetration depth challenges by reducing the EPR frequency, but these experiments are much slower and more complex than traditional MRI due to the need to refresh the DNP-enhanced signal many times over the acquisition time.

We present here a new method for 3D OMRI based on b-SSFP at a constant field of 6.5 mT that provides up to 7-fold acceleration compared to the fastest OMRI sequence reported in the literature (24). We further

[1]Department of Physics, Harvard University, Cambridge, Massachusetts, USA.

[2]Department of Radiology, A.A. Martinos Center for Biomedical Imaging, Massachusetts General Hospital, Boston, Massachusetts, USA.

[3]Department of Radiology, Harvard Medical School, Boston, Massachusetts, USA.

Grant sponsor: Department of Defense, Defense Medical Research and Development Program, Applied Research and Advanced Technology Development Award; Grant number: W81XWH-11-2-0076 (DM09094).

*Correspondence to: Matthew S. Rosen, Ph.D., Low Field MRI and Hyperpolarized Media Laboratory, A. A. Martinos Center for Biomedical Imaging, 149 13th Street, Suite 2301, Charlestown, MA 02129, USA.
E-mail: mrosen@cfa.harvard.edu

Received 30 October 2012; revised 11 January 2013; accepted 7 February 2013.

DOI 10.1002/mrm.24705
Published online 8 March 2013 in Wiley Online Library (wileyonlinelibrary.com).

maintain the high acquisition efficiency of b-SSFP by applying the Overhauser saturation pulses during the phase encode step, eliminating the time-consuming pre-irradiation step done in all previously reported OMRI. Additionally, we add undersampling strategies and compressed sensing (CS) techniques to increase the temporal resolution while also reducing the total number of EPR RF pulses. We obtain $1 \times 2 \times 3.5$ mm^3 resolution on a $54 \times 54 \times 110$ mm^3 sample in 33 s. We show that a steady-state signal is still achieved with this new OMRI b-SSFP sequence, and that simulations with no free parameters agree very well with the experimental results.

METHODS

OMRI Setup

A custom built, low-field MRI scanner with a biplanar 6.5 mT electromagnet (B_0) and biplanar gradients was used for all experiments and was previously described (26) (Fig. 1a). The system was upgraded and optimized for ^{1}H imaging for this work resulting in improved B_0 stability, higher gradient slew rates, and lower overall noise. This effort included the use of an improved power supply (System 854T, Danfysik, Taastrup, Denmark) for the electromagnet with ± 1 ppm stability over 20 min and ± 2 ppm stability over 8 h, and the addition of high-current shielded cables throughout the system. The scanner operates inside a double-screened enclosure (ETS-Lindgren, St. Louis, MO) with a RF noise attenuation factor of 100 dB from 100 kHz to 1 GHz.

The transfer of electron spin polarization to dipolar or scalar coupled nuclear spins via the Overhauser effect requires high power irradiation of the electron spin resonance (27,28). A 7 cm OD, 13 cm long Alderman-Grant coil (29,30; Fig. 1b) with guard rings to reduce sample heating was used to saturate the electron spin resonance of the nitroxide radical 4-hydroxy TEMPO (Sigma-Aldrich, St. Louis, MO). The electron spin resonance is split into three transitions by the hyperfine coupling of the spin 1 ^{14}N nucleus (at 6.5 mT, there still exist other transitions described by the Breit-Rabi equations but their transition probabilities are small and ignored here; 31). As SAR scales with ω^2 (32–36) the EPR coil was tuned to the low energy transition of 140.8 MHz to minimize SAR. The EPR coil was placed inside a 10 cm OD, 16 cm long solenoid coil used for NMR excitation and detection at 276 kHz (Fig. 1c). The coils were oriented such that their B_1 fields were perpendicular to each other and to B_0. Placing the NMR coil outside the ESR coil sacrifices NMR filling factor to gain larger B_1 for electron spin saturation as our DNP signal enhancement (defined as $<I_z>/I_0$ where I_0 is the thermal equilibrium NMR signal and $<I_z>$ is the DNP signal) is limited by the available RF power.

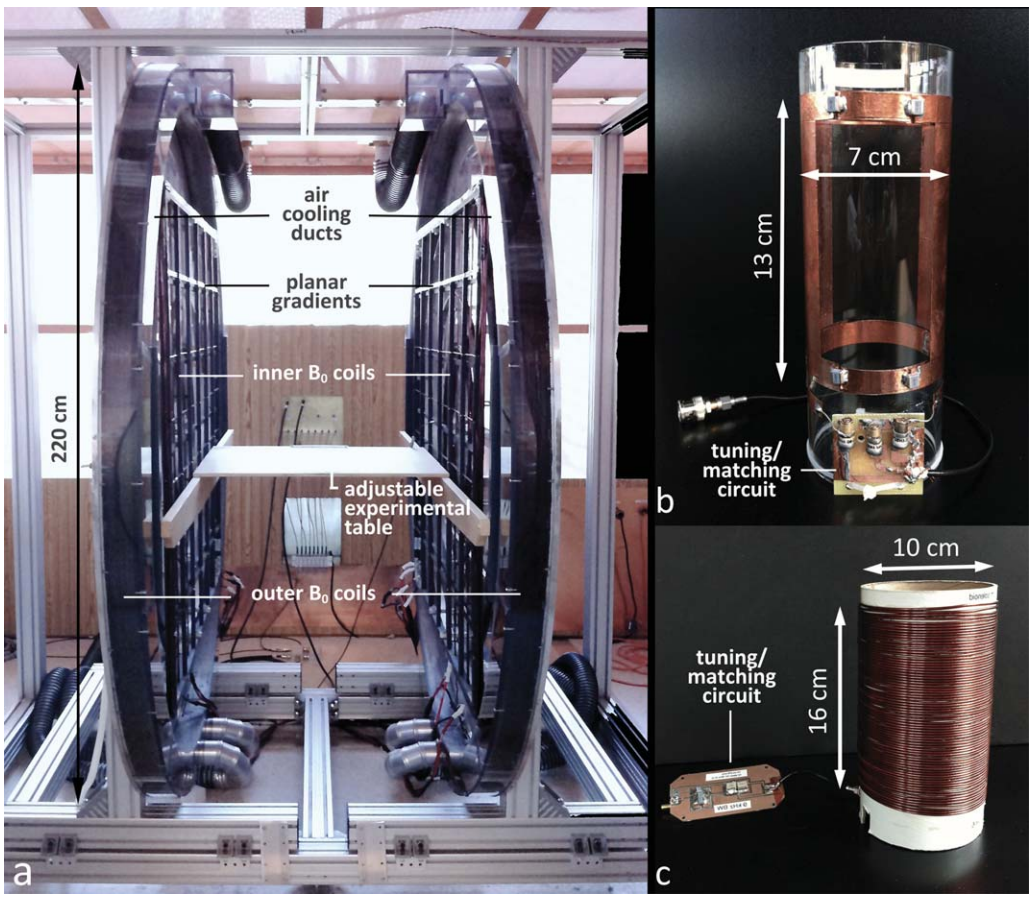

FIG. 1. OMRI setup. Photographs of (**a**) the custom built 6.5 mT MR scanner with bi-planar electromagnet and gradient set inside the shielded room, (**b**) the EPR (141 MHz), and (**c**) NMR (276 kHz) coils used for the OMRI experiments.

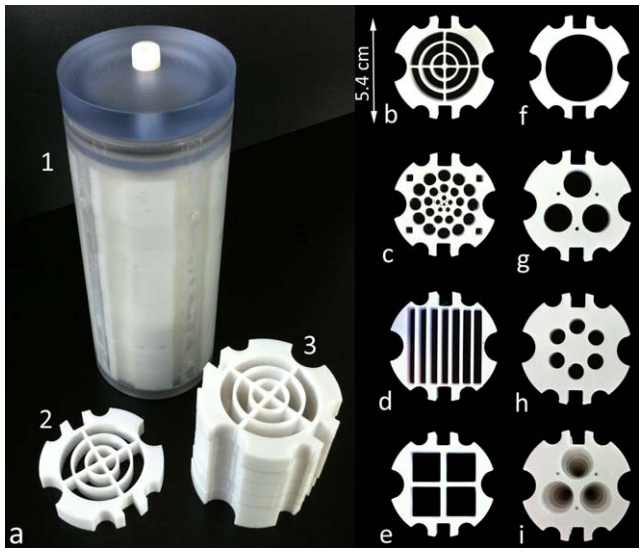

FIG. 2. Photograph of (**a1**) the assembled OMRI phantom, (**a2**) a 10 mm thick internal piece, and (**a3**) a stack of internal pieces. Shown in (**b–h**) are individual pieces of the phantom in configuration 1 (**f–h**) and configuration 2 (**b–e**). A top view of the stacked pieces for the phantom in configuration 1 as described in the text is shown in (**i**). [Color figure can be viewed in the online issue, which is available at wileyonlinelibrary.com.]

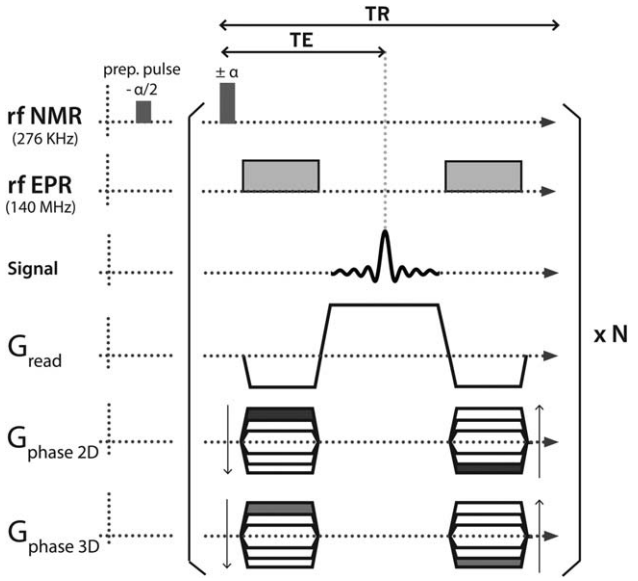

FIG. 3. Diagram of the 3D b-SSFP sequence with embedded EPR pulses (rf EPR). *N* is the total number of TRs in the sequence.

A Redstone NMR console (Tecmag, Houston, TX) was used for data acquisition and controlled the gradients and RF channels. The console has two transmit channels allowing for both NMR and EPR irradiation. A 100 W, CW amplifier (BT00100-DeltaB-CW) was used for EPR saturation and a 500 W pulsed amplifier (BT00500-AlphaS) was used for NMR (from both Tomco Technologies, Stepney, Australia).

Phantom Design

A configurable imaging phantom was built for these experiments. Various pieces designed to demonstrate resolution in three dimensions and test the ability to resolve sharp edges in under-sampled k-space were 3D printed in polycarbonate on a Fortus 360 mc (StrataSys, Eden Prairie, MN). The 3D printed pieces were stacked inside a 5.5 cm ID, 13 cm long machined polycarbonate cylinder. The advantage of this phantom is the flexibility to design and 3D print any desired structure for a particular experiment. The cylinder was then filled with 250 mL of 2.5 mM 4-hydroxy TEMPO solution in water, and a leak-tight polycarbonate cap inserted. The assembled phantom and individual pieces are shown in Figure 2. Imaging experiments were performed in two different phantom stacking configurations. The first stacked geometry consists of two interlocking sets of a trio of stepwise-smooth cones and was used to evaluate the 3D character of the sequence and the minimum structure sizes that can be resolved for round-shaped objects (Fig. 2f–i). The second configuration used more complex structures with finer details to assess the sequence performance, ability to resolve small in-plane structures, and the results of undersampling on sharp edges (Fig. 2b–e). Fiber optic temperature probes (Luxtron, LumaSense Technologies, Santa Clara, CA) were placed inside the phantom and near a ring capacitor on the EPR coil during tests of the imaging sequence to monitor sample and coil temperatures.

3D Balanced SSFP with DNP

The pulse sequence used is shown in Figure 3. It is important to note that there is no separate EPR saturation step unlike all OMRI sequences reported in the literature. The sequence is a b-SSFP sequence with the addition of EPR (Overhauser) irradiation during the balanced phase encode gradients. The b-SSFP excitation train consists of an initial $-\alpha/2$ preparation pulse immediately followed by a train of alternating $\pm\alpha$ excitation pulses as previously described by Sheffler and Lehnhardt (37). The $\pm\alpha$ pulses are separated by TR and the time interval between the $-\alpha/2$ preparation pulse and the first α pulse was set to 2 μs. The main benefit of using a preparation pulse is that it prevents large fluctuations of the pre-steady state signal that would produce image artifacts and thus could not be used for signal acquisition (37). In b-SSFP, the optimal flip angle α is given by $\cos(\alpha) = \frac{T_1/T_2-1}{T_1/T_2+1}$ (37). T_1 and T_2 in our phantom were measured to be 545 ms and 488 ms, respectively, which leads to an optimal flip angle of $\alpha \sim 90^\circ$.

Bloch simulations were performed for a sequence without phase gradients (i.e., at the center of k-space), both with- and without EPR irradiation to model the buildup and time course of transverse magnetization as well as the signal enhancement provided by DNP. The simulations were run in MATLAB (MathWorks, Natick, MA) using code written in-house. Input parameters to the simulations were the measured T_1 and T_2 relaxation times, the measured enhancement provided by DNP with a 1.5 s EPR pulse ($\sim 3 \times {}^1\text{H}\ T_1$) in a 1D spectroscopy experiment (-44.5 fold enhancement), TR/TE = 54/27 ms and $\alpha = 90^\circ$. This negative enhancement results from

Overhauser DNP pumping into the opposite spin nuclear ground state compared with the Boltzmann case. This sign is important for the simulations. OMRI experiments with these parameters, a total bandwidth BW = 9091 Hz, and a 71 Hz bandwidth per pixel, were run and compared with the simulations.

The 3D imaging experiment was performed initially with full Cartesian acquisition of k-space. The sequence was set with TR/TE = 54/27 ms, a 256 × 64 × 112 mm^3 field of view, and acquisition matrix of 128 × 64 × 32, resulting in a 2 × 1 × 3.5 mm^3 voxel size. The balanced phase gradient durations were both set to 20 ms to reach the desired in-plane spatial resolution when the gradient amplifiers were at maximum power. The readout duration was 14 ms with 9091 Hz bandwidth and total acquisition time was 114 s for fully sampled k-space. Critical to the success of these experiments is a very stable magnetic field as off-resonance effects can distort the image and cause severe banding artifacts (37).

It should be noted that the application of EPR saturation pulses while the gradients are on is only possible because our maximum gradient strength is low, 0.1 gauss cm^{-1}, giving a spread in electron resonance frequencies across the 5.5 cm sample (in-plane dimension) of ~1.54 MHz. The loaded Q of the EPR coil was determined using a vector network analyzer and an untuned pick up coil to measure the transmission response of the EPR coil (S21). The measured Q of 62 corresponds to a bandwidth of ~2.3 MHz, thus the spread in electron spin frequencies during the phase encode step is well covered.

Compressed Sensing

Most images are sparse in the sense that they can be accurately represented with fewer coefficients than one would assume given their spectral bandwidth (38). CS is a framework for exploiting sparsity to reconstruct high-fidelity MR images from undersampled k-space datasets that do not fulfill the Nyquist sampling theorem. In CS image reconstruction, image sparsity is enforced by truncating the small coefficients of an object's representation in a sparse basis, typically chosen to be a wavelet transform domain. During image reconstruction, the data are transformed from k-space (the sensing basis) into the wavelet basis via a sparsifying transform, ψ, taken for this work to be the Dirichlet wavelet transform.

CS uses norms to modify the objective function that is optimized during image reconstruction. To understand the role of norms in the objective function, it is helpful to recall standard Fourier reconstruction. For a discrete image m, Fourier operator F, and k-space dataset y, the L_2-norm, $||Fm - y||_2 = (\sum_i |(Fm)_i - y_i|^2)^{1/2}$, is implicitly used to find an image whose Fourier transform differs as little as possible from the k-space data in the Euclidean sense. For fully sampled data, the least squares solution is provided by the Fourier transform. In the case of underdetermined matrix problems (as when the k-space data is undersampled), the L_2-norm may be additionally used to constrain image reconstruction so as to reduce the noise (an approach known as Tikhonov regularization). However, when the L_2-norm is used in this way, it functions as a low-pass filter, penalizing noise at the expense of introducing bias. It does not promote image sparsity. By contrast, the L_1-norm, defined as $||x||_1 = \sum_i |x_i|$ for an arbitrary function x, has a tendency to preserve edges and large coefficients, e.g., for neighboring voxels {0,3,0} the L_2-norm will tend to penalize the difference toward {1,1,1}, while the L_1-norm of both cases is the same, preserving the edge.

The ability of the L_1-norm to preserve large coefficients makes it an appealing choice for enforcing sparsity in images (39,40). In the CS framework, the L_1-norm is applied to the wavelet transform of the image, where it naturally selects the large coefficients representing image features while reducing the small coefficients corresponding to noise and incoherent artifacts. For additional denoising and artifact suppression, a finite difference norm (a discrete implementation of the Total Variation, or *TV*, norm) is applied in the image domain (41). This norm has been shown to preserve object edges while eliminating noise.

As shown in (42), the resulting image reconstruction problem is expressed as a balance between the L_1-norm constraints and the L_2-norm data consistency constraint:

$$\min [||F_u m - y||_2 + \alpha||\psi m||_1 + \beta TV(m)]$$

where F_u is the undersampled Fourier transform operator, y is the undersampled k-space data, and coefficients α and β weight the relative contributions of each norm to the final image. A variety of algorithms are available for minimizing this nonlinear objective function (42). Specific details about our implementation of CS for OMRI b-SSFP are given below.

Undersampled OMRI b-SSFP

The use of CS in MRI relies on the possibility to acquire a priori compressed information and be able to reconstruct the original image as if the latter was fully sampled (42). In the context of data acquisition, this motivates the use of undersampling. CS has been found to work best when k-space is randomly undersampled to produce incoherent artifacts rather than the familiar wrap-around ghosts due to field-of-view contraction when k-space lines are skipped in a regular coherent pattern as is done in conventional parallel imaging (43). For the images presented here, a choice was made to acquire random lines of k-space in the phase-encode directions (k_y, k_z) following a gaussian probability density function. The readout direction was fully sampled. The standard deviations of the sampling pattern as a fraction of the field-of-view along y and z, σ_y, and σ_z, respectively, were adjusted manually to preserve adequate high-frequency information for each undersampling rate. We investigated four undersampling fractions, 50, 70, 80, and 90%. The undersampling patterns are shown in Figure 4. On the acquisition side, this resulted in programming different phase encode tables for each undersampled sequence. The total acquisition time for each undersampling rate is shown in Table 1. To perform image reconstruction according to the L_1-norm and the data consistency constraints, the Sparse MRI code (http://www.eecs.berkeley.edu/~mlustig/Software.html) was used. This code solves the optimization problem using a

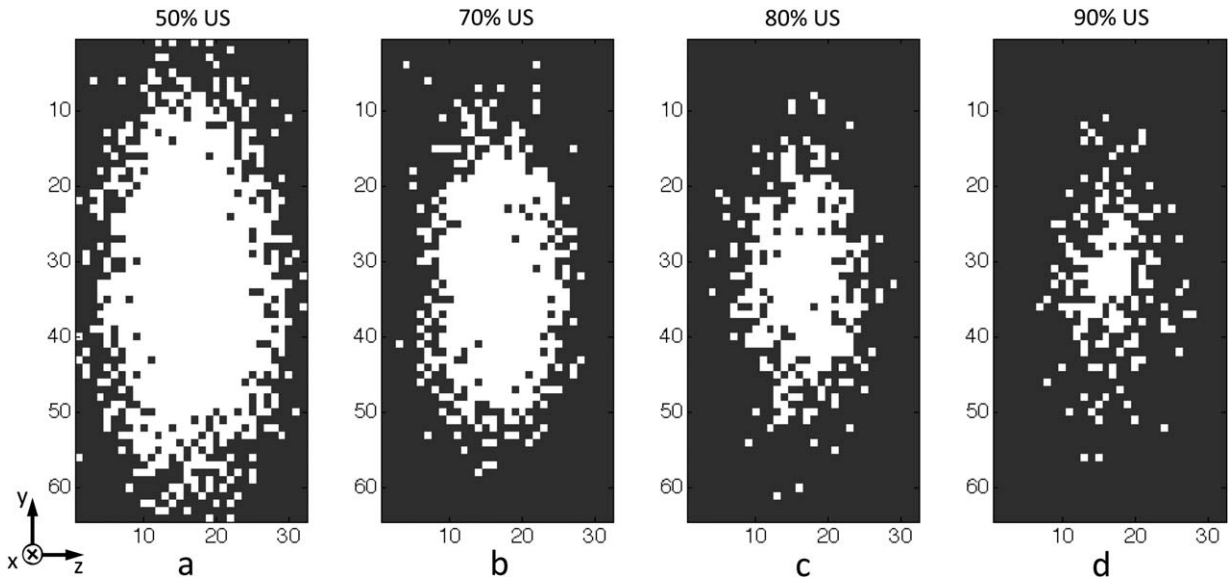

FIG. 4. Undersampling (US) patterns used for (**a**) 50% undersampling, (**b**) 70% undersampling, (**c**) 80% undersampling, and (**d**) 90% undersampling. For an undersampling rate of 50%, 995 of 2048 lines were acquired. For 70% undersampling, 585 of 2048 lines were acquired. For 80% and 90% undersampling, 383 and 185 of 2048 lines were acquired, respectively.

nonlinear conjugate gradient method along with backtracking line-search as described in (42). The parameters for the wavelet and image domain norms were tuned manually to produce low-noise images with preserved object features. The missing values in the acquired k-space data were made identically zero. To separate out the data into slices, a Fourier transform was performed along the readout direction (x). Each sagittal slice of k-space data (y–z plane) was then reconstructed by the Sparse MRI algorithm. After all slices were reconstructed, the resulting 3D block of image domain data was then displayed as transverse (x–y) slices. The computation time for a laptop equipped with a 2.3 GHz quad-core processor was 4.5 min, permitting CS image reconstruction immediately following k-space acquisition.

Table 1
Comparison of Acquisition Time, Maximum SNR, and Mean Absolute Error (MAE) as a Function of the Undersampling Fraction for the Two Different Phantom Configurations with the Maximum Applied RF Power of 62 W at the EPR Coil

	Acq. time (s)	Maximum SNR		MAE
		No CS	CS	
Configuration 1				
Fully sampled	114	23	40.6	
50% Undersampling	56	35.8	75.8	0.073 ± 0.006
70% Undersampling	33	44.6	95	0.072 ± 0.008
80% Undersampling	21	64.3	160	0.112 ± 0.011
90% Undersampling	10	69.8	148	0.149 ± 0.014
Configuration 2				
Fully sampled	114	24.6	42.6	
50% Undersampling	56	30.47	49.7	0.049 ± 0.005
70% Undersampling	33	42	78.3	0.059 ± 0.010
80% Undersampling	21	49.9	94.7	0.100 ± 0.013
90% Undersampling	10	58.1	88.3	0.114 ± 0.014

RESULTS

Steady-State Signal with Embedded EPR Pulses

To understand the approach of transverse magnetization to steady state with embedded EPR pulses in the sequence, Bloch simulations were performed without the phase encode gradients and compared with acquired data. The results are shown in Figure 5. The data was normalized such that the maximum measured signal and the maximum simulated signal were both set to 1. The experimental data with DNP (□) begins at thermal equilibrium, but rapidly builds up to 30 times that of the non-DNP data (○). This build up corresponds to the T_1 relaxation time of the sample (545 ms). The signal reaches ~90% of its steady state value after 24 echoes, or 1.3 s, and the simulation is in good agreement with the data (dashed line; not a fit).

Fully Sampled Versus Undersampled

Images of the two different phantom configurations are shown in Figures 6 and 7 after CS reconstruction. Images reconstructed from fully sampled k-space and from 50, 70, 80, and 90% undersampling are shown. Figure 6a,b shows the top and center structures of the interlocking cones (configuration 1). Figure 6c displays 3D rendered images of the segmented cones for each undersampling fraction. Figure 7a–e shows the different segments of the phantom in configuration 2. For both phantom configurations, 50 and 70% undersampling reproduces the fully sampled images well. Even small structures such as 2 mm diameter holes (Fig. 6a), 1 and 1.5 mm solid separators and 2.5 mm holes (marked by white arrows in Fig. 7b–d) are well resolved at 70% undersampling. For 80 and 90% undersampling, most of the structures are still visible although substantial blurring and ghosting artifacts begin to appear. Figure 7a,e correspond to the top and bottom slice of the phantom and show lower signal

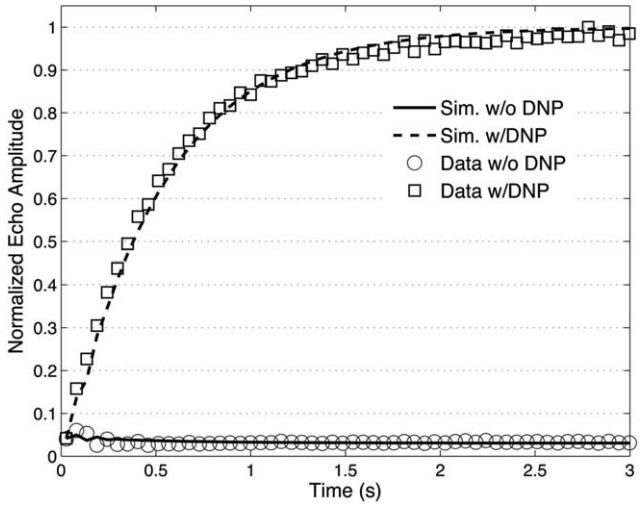

FIG. 5. Simulation and measurement of the approach to steady-state with- and without DNP. Plotted are the echo amplitudes acquired during the pulse sequence in Figure 3 with only the read gradient active. The DNP signal is nearly 30 times larger than the signal without DNP after reaching steady-state. Solid curves plotted are not a fit to the data but an exact simulation with no free parameters as described in the text.

magnitude due to the B_1 profile of the EPR coil. The maximum SNR was calculated from maximal signal amplitudes divided by two times the standard deviation of a user defined noise region before and after CS reconstruction and is shown in Table 1. The increase in SNR with undersampling rate is due to the undersampling pattern acting as an apodization filter that removes high spatial frequencies from k-space. However, all images show an increase in SNR after CS reconstruction. The SNR enhancement using CS increases with the initial SNR of the image and ranges from about 1.5 to 2.5.

To quantify the errors that occur in the undersampled images, the mean absolute error (MAE) was calculated for each image (Table 1). The MAE was calculated by first thresholding the images such that only points that were five times greater than the noise (σ_n) were kept. The undersampled image was then subtracted from the fully sampled image and all non-zero values counted as an error. As seen in Table 1, the MAEs for the 50 and 70% undersampling rates are small and comparable while those for 80 and 90% increase significantly. The MAE for each of the 32 phase encodes gradients along z for configuration 1 is shown in Figure 8 for all undersampling rates. There is little difference across the entire sample between 50 and 70%, again showing that the image is well reproduced with only 30% of the k-space data. Losses in SNR due to the B_1 profile of the EPR coil on slices 1–5 and 25–32 result in increased MAE values for all undersampling rates.

SAR Considerations

A problem limiting the use of OMRI is that the high power RF pulses necessary for DNP lead to high SAR. Two methods were used to estimate SAR. A fiber optic temperature probe was placed inside the sample and the fully sampled k-space sequence was run several times, waiting several minutes in between runs to allow the

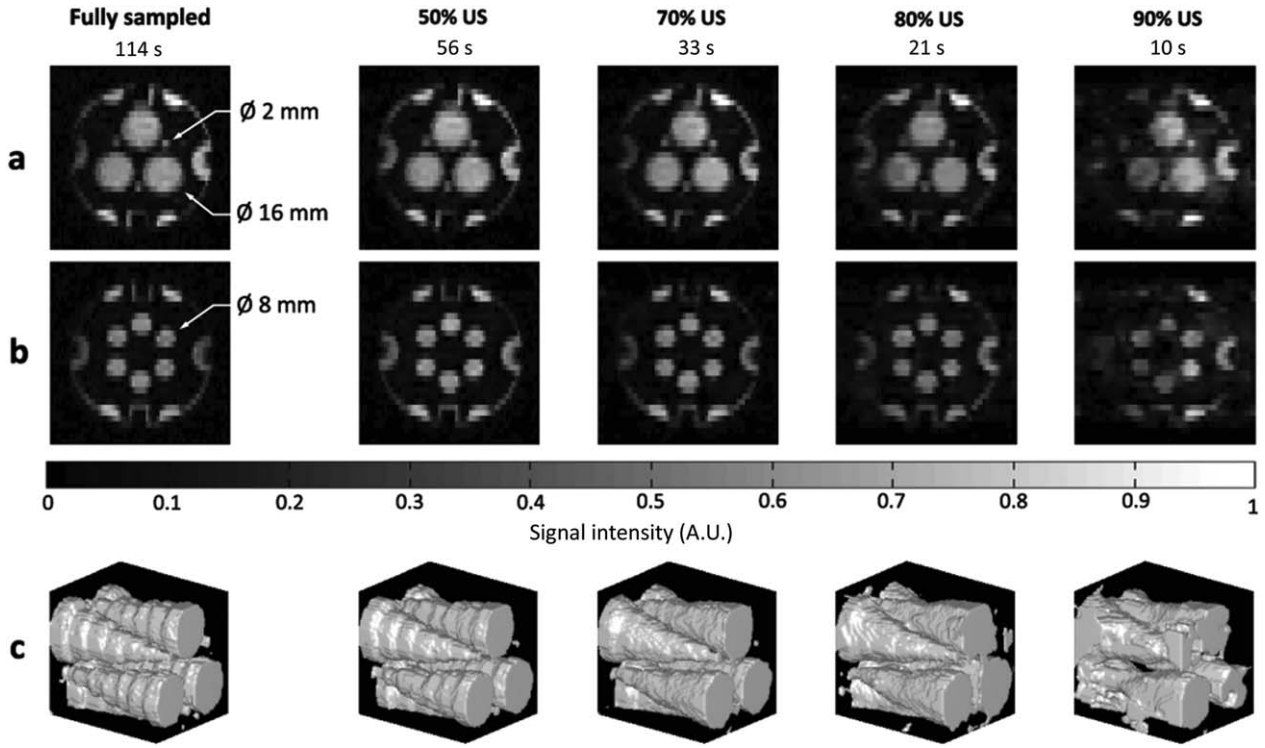

FIG. 6. Fully and undersampled (US) images of the phantom in configuration 1 after CS reconstruction as a function of undersampling fraction. a: Representative slices: Top (**a**) and center (**b**) of the full 32 slice dataset. Acquisition matrix: 128 × 64 × 32, voxel size: 2 × 1 × 3.5 mm^3. **c**: 3D rendered images of the interlocked cone structure obtained from the fully and undersampled datasets.

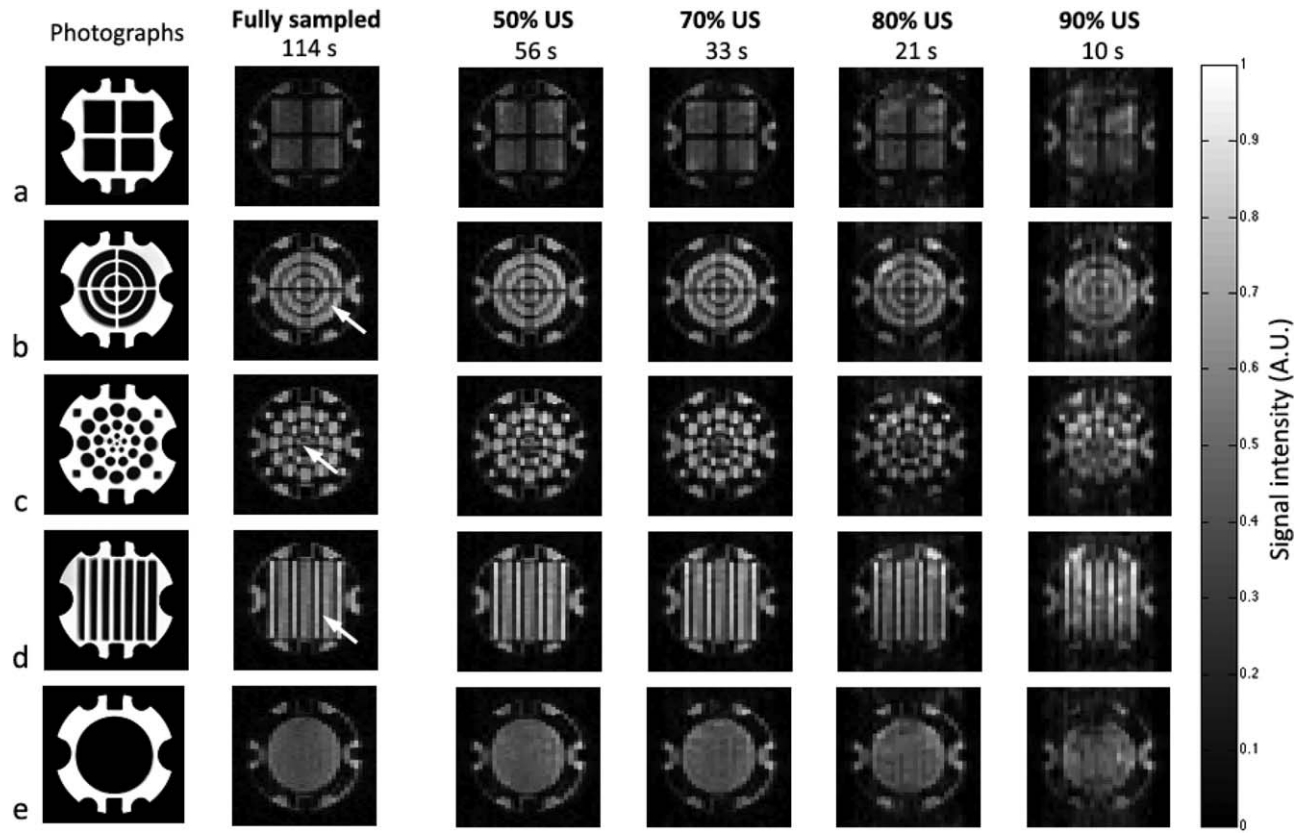

FIG. 7. Fully and undersampled (US) images of five representative slices after CS reconstruction. The full 32-slice data set was acquired with the phantom in configuration 2 as described in the text. MR images are shown alongside photographs of the corresponding phantom piece. Acquisition matrix: 128 × 64 × 32, voxel size: 2 × 1 × 3.5 mm^3. White arrows indicate 1 and 1.5 mm solid separators, (**b**) and (**d**), respectively, and 2.5 mm diameter structures (**c**).

EPR coil to cool. The maximum measured temperature increase was 0.4°C. No temperature increase was measured for any of the undersampled sequences. Estimating SAR $\sim cT/\Delta t$ (44) where c is the specific heat, ΔT is the temperature change and Δt is the time of the sequence gives SAR = 15 W kg^{-1}. We expect this to represent a lower limit as heat may have dissipated during the sequence. As a second method, the power dissipated in the sample was estimated using (45):

$$P_{\text{sample}} = P_{\text{coil}}(1 - Q_{\text{loaded}}/Q_{\text{unloaded}})$$

The forward power was measured using a directional coupler (Model 3020A, Narda Microwave, Hauppauge, NY) and power meter (V3500A, Agilent Technologies, Santa Clara, CA), and the maximum forward power to the coil was ~62 W. The loaded Q was measured to be 52 while the unloaded Q was 62. Thus the power to the sample during an EPR pulse is ~10 W. The EPR irradiation is on for 73% of TR and the sample mass is 0.25 kg, therefore SAR = 29 W kg^{-1}.

The 50% undersampled images in Figures 6 and 7 have high SNR and accurately represent the phantom. Therefore, we reduced the forward power to the coil by factors of 2, 4, 8, and 16 to investigate how much the SAR could be reduced (thusly reducing the Overhauser enhancement) while maintaining high image quality. The results are shown in Figure 9 and Table 2. Image quality is well maintained for 31 and 15.5 W forward power corresponding to an estimated SAR of ~14.5 and 7.25 W kg^{-1}, respectively.

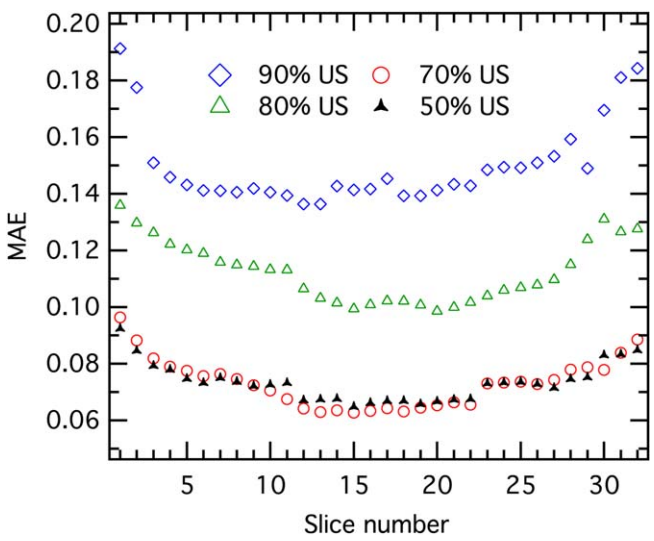

FIG. 8. MAE computed each slice number for each undersampling fraction with the phantom in configuration 1: 50% US (black), 70% US (red), 80% US (green), and 90% US (blue). [Color figure can be viewed in the online issue, which is available at wileyonlinelibrary.com.]

DISCUSSION

The 3D Overhauser-enhanced b-SSFP sequence presented here in combination with CS and undersampling techniques allows us to attain $1 \times 2 \times 3.5$ mm^3 voxel size in our phantom in 33 s (70% undersampling in Figs. 6 and 7) at 6.5 mT. The resulting CS reconstructed image is nearly identical to the original fully sampled image and has ~2 times higher SNR. This was achieved by inserting the EPR saturation pulses within TR during the prephase/rephase gradients, thus removing the time consuming prepolarization step as in other OMRI sequences. As shown in our experiments and simulations (Fig. 5), a large steady-state signal is quickly reached with 90% of the maximum signal reached in <1.5 s, and constant polarization in the sample is maintained during the remainder of the acquisition. This eliminates the need to correct acquisitions for T_1 decay and to rectify undesirable phase shifts that can occur when using prepolarization techniques (25,46). The maximum signal with b-SSFP at thermal equilibrium is given by $M_{ss} = \frac{1}{2} M_0 \sqrt{T_2/T_1} = 0.47 M_0$ (37). Overhauser saturation pulses during the phase gradient increases M_{SS} by ~30 for the sample used here, thus allowing high SNR images comparable to those obtained with conventional OMRI techniques. The simulations provide a reliable tool to optimize the phase encode gradient durations depending on T_1 and T_2.

The application of EPR saturation pulses during the balanced phase encode gradient events is our first major source of acceleration. This allows us to acquire images twice as fast as spin echo OMRI sequences recently published in the literature (24) with nearly seven times higher spatial resolution ($1 \times 2 \times 3.5$ mm^3 vs. $1.25 \times 1.25 \times 30$ mm^3). This is possible by covering the spread in electron spin frequencies in the phantom when the maximum 0.1 gauss cm^{-1} phase encode gradient was turned on. This sets an upper limit on the Q factor of the EPR coil, or alternatively, the maximum gradient strength that can be used for these experiments. While the maximum steady-state DNP enhancements would benefit from a higher Q coil, the goal of maintaining nearly constant signal enhancement across the sample during imaging would suffer. However, when the EPR irradiation occurs as separate step before imaging as in other OMRI sequences, the DNP signal is also not constant across the image due to the decay of polarization, so a compromise of higher gradient strength for uneven DNP polarization may be acceptable.

Partial sampling of k-space (and subsequent reconstruction via CS) is our second major acceleration factor. In the case of 70% undersampling, this result in additional 3.5 fold acceleration while keeping the voxel size unchanged, thus resulting in seven times faster acquisition compared with recently published work (24). By undersampling in each phase encode direction according to a gaussian probability density function, the center of k-space is emphasized, preserving image contrast without completely sacrificing the high frequency information at the edge of k-space. However, the choice of the lines sampled in k-space was empirically determined and only a few undersampling patterns were empirically tested for a given undersampling rate. The degrees of freedom in the generation of underspampling patterns is large (choice of lines sampled, $\sigma_{y,z}$) and a large number of combinations could have been tested with the opportunity to give even better results. However, for the $\sigma_{y,z}$'s used here, the 50% and 70% undersampling rates accurately reproduced the image for different random samplings of k-space. In addition, this work focuses on Cartesian sampling, but alternative sampling trajectories (spiral and radial) have been shown to offer more flexibility in the design of 3D incoherent sampling sequences that are particularly well for the use of CS techniques (47–50).

CS performs natural denoising, bringing an improvement in SNR. Incoherent artifacts resulting from subsampled k-space are efficiently suppressed using L_1-norm constraints in the image and wavelet domains as previously detailed in the literature (42). However, more than 70% undersampling could not provide satisfying reconstruction in spite of high SNR. The incorporation of prior knowledge (51–53) in the image reconstruction process could overcome this limitation by partially recovering irretrievable loss of information caused by heavy undersampling and further increase our temporal resolution. In addition, it is important to note that the 4.5 min computation time required for the CS reconstruction does not significantly penalize the time saved from undersampling.

The gain in temporal resolution obtained here for 70% undersampling, around 1 s per acquired slice, provides new insight for investigating cases where high temporal resolution is needed, such as monitoring the concentration change, oxidation, and metabolism of free radicals that correlate directly with organ functions and tissue health. In addition, shorter durations for the read and phase encode gradients could have been implemented to give significantly shorter acquisition times but at the cost of a decreased spatial resolution. Likewise, doubling the gradient strength in read and both phase encode directions would allow us to reach 2^3 times higher spatial resolution for a fixed acquisition time.

Considering the SAR resulting from the sequence, the amount of power sent to the EPR coil was decreased by a factor of 4 while still keeping the SNR >25. Even if a compromise has to be found between the desired spatial resolution of the image and sample heating due to the high power RF, the total amount of RF power sent to the sample during imaging is considerably reduced by the use of undersampling strategies. No temperature rise was measured in the sample for the 50 to 90% undersampling fractions with the maximum EPR power used in this study. With the maximum available EPR power, we acquired images with an in-plane resolution of 1×1 mm^2 as shown in Figure 10 with 70% undersampling (while maintaining the 3.5 mm slice thickness). Total acquisition time was 65 s. This image displays excellent in-plane resolution with very little blurring of the 1 mm features and high SNR.

The images presented here were acquired with a sufficiently long TR to obtain the desired in-plane resolution while keeping the gradient strength low enough for

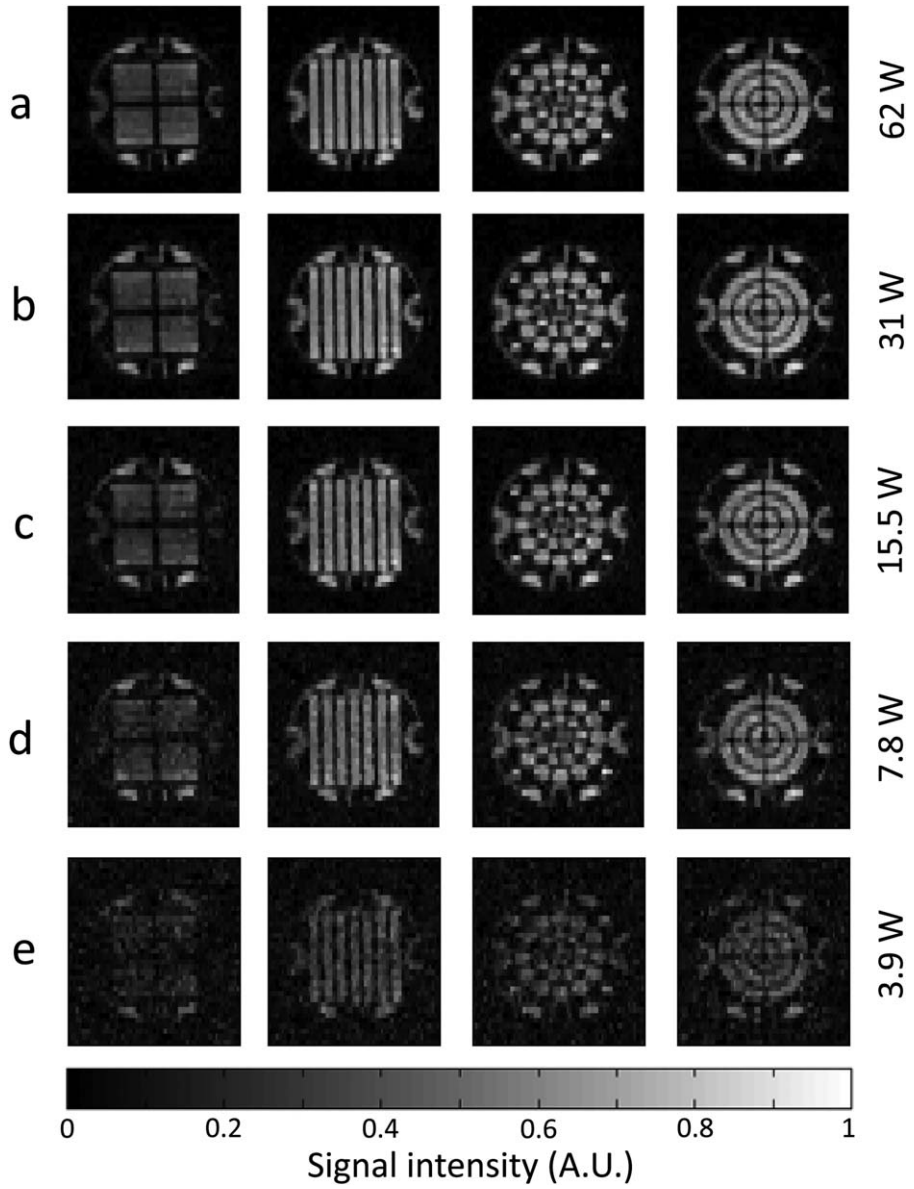

FIG. 9. Images taken with the phantom in configuration 2 and 50% undersampling as a function of Overhauser drive power: (**a**) 62 W, (**b**) 31 W, (**c**) 15.5 W, (**d**) 7.8 W, and (**e**) 3.9 W EPR power. Acquisition matrix: 128 × 64 × 32, voxel size: 2 × 1 × 3.5 mm^3, and TR/TE: 54/27 ms. Total acquisition time per image was 56 s.

efficient EPR saturation during phase encoding. We note that the phantom used here has significantly longer T_2 and T_1 relaxation times than would be expected for in vivo applications. Bloch simulations were run to estimate how the current sequence would perform with relaxation times 10 times shorter than the phantom used here. Keeping all simulation parameters as in Figure 5, but decreasing T_1 to 55 ms and T_2 to 49 ms resulted in <15% reduction in signal intensity (compared with the dashed line in Figure 5). While relaxation times comparable to TR tend to reduce signal, this is partially offset by a faster approach to steady state. More likely to hamper the effectiveness of OMRI in vivo, however, is a decrease in the maximum DNP signal enhancement due to extra ^{1}H nuclear spin relaxation pathways that compete with relaxation caused by dipolar coupling to the electron spin (27). To observe this effect, simulations were run with the short T_1 and T_2 times above while decreasing the maximum DNP signal enhancement to −10 and −5. This reduced the steady state signal intensity by 80 and 90%, respectively, compared with the dashed line in Figure 5. Although the signal is much smaller, it is still a factor of 7 and 3.5 times larger than the thermal equilibrium signal with the same parameters, and therefore still provides very useful contrast. In the case of injected free radical detection, this decrease in signal can be partially overcome by increasing the free radical concentration. For example, injection of 0.6 mL

Table 2
The Maximum SNR as a Function of Power at the EPR Coil with and without CS for the Phantom in Configuration 2

	Max. SNR	
Power to EPR coil (W)	No CS	CS
62	36	75
31	29.3	48
15.5	21	26.4
7.8	15.2	18.2
3.9	11.4	16.2

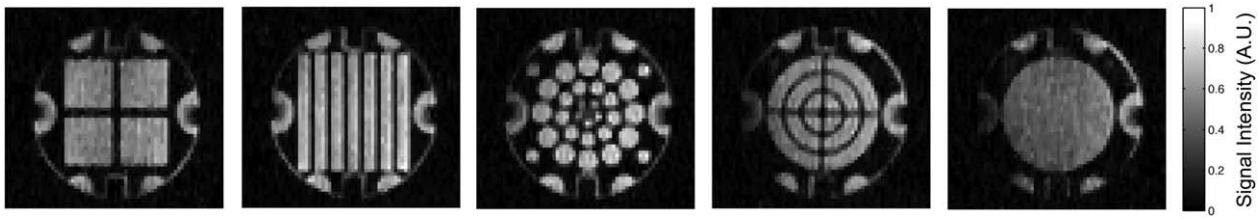

FIG. 10. High-resolution CS reconstructed images taken in the phantom in configuration 2 (five slices are shown) with 70% undersampling. Acquisition matrix: 256 × 64 × 32, voxel size: 1 × 1 × 3.5 mm^3, and TR/TE: 54/27 ms. Total acquisition time was 65 s.

of 100 mM nitroxide radical in mice has been reported in recent work (24). Assuming 60–80 mL of blood per kg of bodyweight (54), the dilution factor is between 3 and 4 for a 30 g mouse, resulting in a nominal 29 mM free radical concentration, more than 10 times higher than the 2.5 mM used in the work presented here.

CONCLUSION

We have demonstrated a new strategy for fast high-resolution 3D Overhauser MRI using b-SSFP in a phantom containing 2.5 mM 4-hydroxy TEMPO solution at 6.5 mT. The embedding of EPR excitation pulses directly into the b-SSFP sequence eliminates the prepolarization step used in other OMRI sequences, reducing the acquisition time and obviating the need for long, high power RF EPR pulses. The use of undersampling strategies and CS reconstruction algorithms further reduces imaging time. We have shown that an undersampling rate of 70% gives unperceivable reconstruction errors when compared with the fully sampled data sets, allowing the acquisition of 32 slices in our phantom volume within 33 s. This work overcomes the main limitations of Overhauser enhanced MRI as previously described in the literature, drastically improving speed and resolution, and enabling new opportunities for the measurement of free radicals in living organisms, and for the study of dynamic processes such as metabolism and flow.

ACKNOWLEDGMENTS

The authors thank Ronald Walsworth and Stephen DeVience for assistance with relocating and upgrading the low-field scanner, Jennifer McNab and Thomas Witzel for valuable discussions on implementing b-SSFP sequences at 6.5 mT, and David Donoho and Michael Lustig for sharing the package wavelet toolbox (Wavelab) online with the scientific community.

REFERENCES

1. Ardenkjaer-Larsen JH, Laursen I, Leunbach I, Ehnholm G, Wistrand LG, Petersson JS, Golman K. EPR and DNP properties of certain novel single electron contrast agents intended for oximetric imaging. J Magn Reson 1998;133:1–12.
2. James PE, Madhani M, Roebuck W, Jackson SK, Swartz HM. Endotoxin-induced liver hypoxia: defective oxygen delivery versus oxygen consumption. Nitric Oxide 2002;6:18–28.
3. Ahn KH, Scott G, Stang P, Conolly S, Hristov D. Multiparametric imaging of tumor oxygenation, redox status, and anatomical structure using overhauser-enhanced MRI–prepolarized MRI system. Magn Reson Med 2011;65:1416–1422.
4. Lurie DJ, Davies GR, Foster MA, Hutchison JMS. Field-cycled PEDRI imaging of free radicals with detection at 450 mT. Magn Reson Imaging 2005;23:175–181.
5. Massot P, Parzy E, Pourtau L, Mellet P, Madelin G, Marque S, Franconi J-M, Thiaudiere E. In vivo high-resolution 3D Overhauser-enhanced MRI in mice at 0.2 T. Contrast Media Mol Imaging 2012;7:45–50.
6. Kosem N, Naganuma T, Ichikawa K, Phumala Morales N, Yasukawa K, Hyodo F, Yamada K-I, Utsumi H. Whole-body kinetic image of a redox probe in mice using Overhauser-enhanced MRI. Free Radic Biol Med 2012;53:328–386.
7. Caia GL, Efimova OV, Velayutham M, El-Mahdy MA, Abdelghany TM, Kesselring E, Petryakov S, Sun Z, Samouilov A, Zweier JL. Organ specific mapping of in vivo redox state in control and cigarette smoke-exposed mice using EPR/NMR co-imaging. J Magn Reson 2012;216:21–27.
8. Mellet P, Massot P, Madelin G, Marque SRA, Harte E, Franconi J-M, Thiaudiere E. New concepts in molecular imaging: non-invasive MRI spotting of proteolysis using an overhauser effect switch. PLoS One 2009;4:e5244.
9. Halpern HJ, Chandramouli GV, Barth ED, Yu C, Peric M, Grdina DJ, Teicher BA. Diminished aqueous microviscosity of tumors in murine models measured with in vivo radiofrequency electron paramagnetic resonance. Cancer Res 1999;59:5836–5841.
10. Barros W, Engelsberg M. Enhanced Overhauser contrast in proton-electron double-resonance imaging of the formation of an alginate hydrogel. J Magn Reson 2007;184:101–107.
11. Eaton GR, Eaton SS, Ohno K. EPR imaging and in vivo EPR. Boca Raton: CRC Press; 1991.
12. Kuppusamy P, Chzhan M, Zweier J. Principles of imaging. In: Berliner LJ, editor. Biological magnetic resonance, Vol. 18. In vivo EPR (ESR): theory and applications. New York: Kluwer Academic/Plenum Publishers; 2003. p 99–152.
13. Halpern HJ, Yu C, Peric M, Barth ED, Karczmar GS, River JN, Grdina DJ, Teicher BA. Measurement of differences in pO2 in response to perfluorocarbon/carbogen in FSa and NFSa murine fibrosarcomas with low-frequency electron paramagnetic resonance oximetry. Radiat Res 1996;145:610–618.
14. Halpern HJ, Yu C, Peric M, Barth E, Grdina DJ, Teicher BA. Oxymetry deep in tissues with low-frequency electron paramagnetic resonance. Proc Natl Acad Sci USA 1994;91:13047–13051.
15. Subramanian S, Yamada K-I, Irie A, Murugesan R, Cook JA, Devasahayam N, Van Dam GM, Mitchell JB, Krishna MC. Noninvasive in vivo oximetric imaging by radiofrequency FT EPR. Magn Reson Med 2002;47:1001–1008.
16. Velayutham M, Li H, Kuppusamy P, Zweier JL. Mapping ischemic risk region and necrosis in the isolated heart using EPR imaging. Magn Reson Med 2003;49:1181–1187.
17. He G, Samouilov A, Kuppusamy P, Zweier JL. In vivo imaging of free radicals: applications from mouse to man. Mol Cell Biochem 2002;234/235:359–367.
18. Lurie DJ, Bussell DM, Bell LH, Mallard JR. Proton-electron double magnetic resonance imaging of free radical solutions. J Magn Reson 1988;76:366–370.
19. Golman K, Petersson JS, Ardenkjaer-Larsen JH, Leunbach I, Wistrand LG, Ehnholm G, Liu K. Dynamic in vivo oxymetry using overhauser enhanced MR imaging. J Magn Reson Imaging 2000;12:929–938.
20. Krishna MC, English S, Yamada K, et al. Overhauser enhanced magnetic resonator imaging for tumor oximetry: coregistration of tumor anatomy and tissue oxygen concentration. Proc Natl Acad Sci USA 2002;99:2216–2221.

21. Utsumi H, Yamada K-I, Ichikawa K, Sakai K, Kinoshita Y, Matsumoto S, Nagai M. Simultaneous molecular imaging of redox reactions monitored by Overhauser-enhanced MRI with 14N- and 15N-labeled nitroxyl radicals. Proc Natl Acad Sci USA 2006;103:1463–1468.
22. Li H, He G, Deng Y, Kuppusamy P, Zweier JL. In vivo proton electron double resonance imaging of the distribution and clearance of nitroxide radicals in mice. Magn Reson Med 2006;55:669–675.
23. Benial AM, Ichikawa K, Murugesan R, Yamada K, Utsumi H. Dynamic nuclear polarization properties of nitroxyl radicals used in Overhauser-enhanced MRI for simultaneous molecular imaging. J Magn Reson 2006;182:273–282.
24. Sun Z, Li H, Petryakov S, Samouilov A, Zweier JL. In vivo proton electron double resonance imaging of mice with fast spin echo pulse sequence. J Magn Reson Imaging 2012;35:471–475.
25. Youngdee W, Lurie DJ, Foster MA. Rapid imaging of free radicals in vivo using hybrid FISP field-cycled PEDRI. Phys Med Biol 2002;47:1091–1100.
26. Tsai LL, Mair RW, Rosen MS, Patz S, Walsworth RL. An open-access, very-low-field MRI system for posture-dependent 3He human lung imaging. J Magn Reson 2008;193:274–285.
27. Hausser KH, Stehlik D. Dynamic nuclear polarization in liquids. Adv Magn Reson 1968;3:79–139.
28. Muller-Warmuth W, Meise-Gresch K. Molecular motions and interactions as studied by dynamic nuclear polarization (DNP) in free radical solutions. Adv Magn Reson 1983;11:1–45.
29. Alderman DW, Grant DM. An efficient decoupler coil design which reduces heating in conductive samples in superconducting spectrometers. J Magn Reson 1979;36:447–451.
30. Lurie DJ, Li H, Petryakov S, Zweier JL. Development of a PEDRI free-radical imager using a 0.38 T clinical MRI system. Magn Reson Med 2002;47:181–186.
31. Rabi II, Zacharias JR, Millman S, Kusch P. A new method of measuring nuclear magnetic moment. Phys Rev 1938;53:318.
32. Bottomley PA, Andrew ER. RF magnetic field penetration, phase shift and power dissipation in biological tissue: implications for NMR imaging. Phys Med Biol 1978;23:630–643.
33. Jin J. Electromagnetic analysis and design in magnetic resonance imaging. Boca Raton, FL: CRC Press; 1998.
34. Collins CM, Li S, Smith MB. SAR and B1 field distributions in a heterogeneous human head model within a birdcage coil. Specific energy absorption rate. Magn Reson Med 1998;40:847–856.
35. Collins CMC, Smith MBM. Calculations of B(1) distribution, SNR, and SAR for a surface coil adjacent to an anatomically-accurate human body model. Magn Reson Med 2001;45:692–699.
36. Collins CM, Wang Z. Calculation of radiofrequency electromagnetic fields and their effects in MRI of human subjects. Magn Reson Med 2011;65:1470–1482.
37. Scheffler K, Lehnhardt S. Principles and applications of balanced SSFP techniques. Eur Radiol 2003;13:2409–2418.
38. Candes EJ, Romberg J, Tao T. Robust uncertainty principles: exact signal reconstruction from highly incomplete frequency information. IEEE Trans Inform Theory 2006;52:489–509.
39. Donoho DL. Compressed sensing. IEEE Trans Inform Theory 2006;52:1289–1306.
40. Candes EJ, Wakin MB. An introduction to compressive sampling. IEEE Signal Process Mag 2008;25:21–30.
41. Rudin LI, Osher S, Fatemi E. Nonlinear total variation based noise removal algorithms. Phys D: Nonlinear Phenom 1992;60:259–268.
42. Lustig M, Donoho D, Pauly JM. Sparse MRI: the application of compressed sensing for rapid MR imaging. Magn Reson Med 2007;58:1182–1195.
43. Pruessmann KP, Weiger M, Scheidegger MB, Boesiger P. SENSE: sensitivity encoding for fast MRI. Magn Reson Med 1999;42:952–962.
44. Oh S, Webb AG, Neuberger T, Park B, Collins CM. Experimental and numerical assessment of MRI-induced temperature change and SAR distributions in phantoms and in vivo. Magn Reson Med 2010;63:218–223.
45. Matsumoto S, Yamada K, Hirata H, Yasukawa K, Hyodo F, Ichikawa K, Utsumi H. Advantageous application of a surface coil to EPR irradiation in overhauser-enhanced MRI. Magn Reson Med 2007;57:806–811.
46. Puwanich P, Lurie DJ, Foster MA. Rapid imaging of free radicals in vivo using field cycled PEDRI. Phys Med Biol 1999;44:2867–2877.
47. Lustig M, Lee J, Donoho D, Pauly J. Faster imaging with randomly perturbed, undersampled spirals and L1 reconstruction. In Proceedings of the 13th Annual Meeting of ISMRM, Miami Beach, Florida, USA, 2005. p. 155.
48. Santos JM, Cunningham CH, Lustig M, Hargreaves BA, Hu BS, Nishimura DG, Pauly JM. Single breath-hold whole-heart MRA using variable-density spirals at 3T. Magn Reson Med 2006;55:371–379.
49. Ye JC, Tak S, Han Y, Park HW. Projection reconstruction MR imaging using FOCUSS. Magn Reson Med 2007;57:764–775.
50. Block KT, Uecker M, Frahm J. Undersampled radial MRI with multiple coils. Iterative image reconstruction using a total variation constraint. Magn Reson Med 2007;57:1086–1098.
51. Mistretta CA, Wieben O, Velikina J, Block W, Perry J, Wu Y, Johnson K, Wu Y. Highly constrained backprojection for time-resolved MRI. Magn Reson Med 2005;55:30–40.
52. Chen G-H, Tang J, Leng S. Prior image constrained compressed sensing (PICCS): a method to accurately reconstruct dynamic CT images from highly undersampled projection data sets. Med Phys 2008;35:660–663.
53. Lauzier PT, Tang J, Chen G-H. Prior image constrained compressed sensing: implementation and performance evaluation. Med Phys 2012;39:66–80.
54. Sluiter W, Oomens LWM, Brand A, Van Furth R. Determination of blood volume in the mouse with 51Chromium-labelled erythrocytes. J Immunol Methods 1984;73:221–225.